GROUND-RADAR NUMERICAL MODELING APPLIED TO ENGINEERING PROBLEMS

JOSÉ M. CARCIONE

Osservatorio Geofisico Sperimentale, P.O. Box 2011 Opicina, 34016 Trieste, Italy.

ABSTRACT

Carcione, J.M., 1996. Ground-radar numerical modeling applied to engineering problems. *European Journal of Environmental and Engineering Geophysics*, 1: 65-81.

This paper presents two engineering applications of a novel forward-modeling algorithm for the simulation of georadargrams. The method is based on the solution of the time-domain Maxwell equations by a direct grid method. The standard TM differential equations are modified in order to include out-of-phase conduction currents (that contribute to the effective permittivity) and dielectric attenuation processes, such as free and bound water relaxation. This is achieved by assuming time-dependent conductivity and permittivity functions that are represented, in terms of analogous mechanical models, by a Kelvin-Voigt element and a Zener relaxation function, respectively. The convolution integral introduced by the relaxation formulation is circumvented by defining new *hidden* field variables that correspond to dielectric relaxation processes. The equations are solved numerically by using the Fourier pseudospectral operator for computing the spatial derivatives, and a new time-splitting integration algorithm that obviates the stiffness of the differential equations.

The two applications illustrate the potential of the modeling algorithm. In the first simulation, a radargram corresponding to three cylindrical objects is computed. Since the objects are small compared with the dominant wavelength of the electromagnetic pulse, they act as secondary sources, according to Huygens' principle, thus generating typical hyperbolic responses. Despite the small size of the cylinders, the effects of the material composition can be observed in the amplitude and phase of the reflected wavefields.

The second model represents an old concrete road overlying a cavity. The different layers and the cavity, which is 30 cm deep, can be resolved with a 850 MHz transmitting antenna but not with a 500 Mhz antenna. Moreover, the influence of the water relaxation phenomenon is analyzed by considering the cavity filled with salt water. Its presence strongly attenuates the reflections generated at the bottom of the cavity and at the layers below.

KEY WORDS: ground-penetrating radar, modeling, dielectric relaxation, cavity, road.

INTRODUCTION

During the last decade, ground-penetrating radar (GPR) has become an important shallow subsurface exploration tool [for a recent review see Owen (1995)]. This high-frequency EM technique is conceptually similar to the seismic reflection method (Carcione and Cavallini, 1995) and, therefore, many of the algorithms used in oil exploration can be applied, with minor modification, to the interpretation of georadargrams. In particular, forward modeling in heterogeneous media is essential to validate the interpretation. GPR wave modeling in the literature is, in general, one-dimensional. Only very recently, has Goodman (1994) proposed a two-dimensional wave simulation method based on ray-tracing techniques, but his modeling suffers the disadvantages of asymptotic ray methods.

It is important to model the correct frequency dependence of the permittivity and the conductivity. At radar frequencies ($\approx$ 50 MHz - 2 GHz), various dielectric dispersion processes occur. Fig. 9.1 of Hasted (1973) is a good illustration of the various contributions to the dielectric loss in moist soils. The most important are ionic conductivity, bound and free water relaxation, and the Maxwell-Wagner effect. The relaxation of the water molecule produces an increase in attenuation with frequency, since the molecules begin to lag the applied field and increase the real effective conductivity. This phenomenon is well described by a Debye relaxation peak, having its analogy in the Zener rheological model used in viscoelasticity (Carcione et al., 1988). Other, less important processes that can be described by Debye mechanisms are, the Maxwell-Wagner effect, and surface conductivity at low frequencies. Moreover, at high frequencies, the response of free charges may lag the electric field and produce an out-of-phase component, contributing to the real effective permittivity. These phenomena, i.e., dielectric relaxation and out-of-phase electric currents, are introduced into the Maxwell equations by means of time-domain permittivity and conductivity functions.

THE RADAR EQUATIONS

The modeling described in this paper assumes that the propagation is in the (x,z)-plane, and that the material properties are constant with respect to the y-coordinate. Then, the electric and magnetic field components E_x, E_z and H_y are decoupled from E_y, H_x and H_z. The first three fields obey the TM (Transverse Magnetic) differential equations:

$$(\partial E_z/\partial x) - (\partial E_x/\partial z) = \mu_0(\partial H_y/\partial t) + M_y \quad , \tag{1}$$

$$-\partial H_y/\partial z = \sigma^*(\partial E_x/\partial t) + \epsilon^*(\partial^2 E_x/\partial t^2) + J_x \quad , \tag{2}$$

$$\partial H_y/\partial x = \sigma^*(\partial E_z/\partial t) + \epsilon^*(\partial^2 E_z/\partial t^2) + J_z \quad , \tag{3}$$

where $\epsilon(t)$ and $\sigma(t)$ are the permittivity and conductivity functions, μ_0 is the free-space magnetic permeability, J and M are the electric and magnetic current densities respectively, and the symbol * denotes time convolution.

A realistic description of the permittivity is obtained by using a Debye model, also called Zener or standard linear solid model (Zener, 1948). This model accounts for many relaxation mechanisms, producing an out-of-phase component of the permittivity that contributes to the effective conductivity. For instance, one dielectric relaxation process is described by

$$\epsilon(t) = \epsilon^0[1 - (1-\lambda/\tau)\exp(-t/\tau)] \, H(t) \quad , \tag{4}$$

where ϵ^0 is the static permittivity, λ and τ are relaxation times ($\lambda \leq \tau$), and H(t) is the Heaviside function. The optical or high-frequency permittivity is obtained for $t \to 0$: $\epsilon^\infty = (\lambda/\tau)\epsilon^0$ (note that $\epsilon^\infty \leq \epsilon^0$).

In contrast, the conductivity components are represented by a Kelvin Voigt mechanical model analogue:

$$\sigma(t) = \sigma^0[H(t) + \xi\delta(t)] \quad , \tag{5}$$

where σ^0 is the static conductivity, ξ is a relaxation time, and $\delta(t)$ is the Dirac function. The out-of-phase component of the conduction current is quantified by the relaxation time ξ.

The TM equations (1), (2) and (3) could provide the basis for a numerical solution algorithm, however, the numerical evaluation of the convolution integrals is impractical when solving the differential equations with grid methods and explicit time-evolution techniques. The conductivity terms pose no problems, since the substitution of the conductivity function (5) into Maxwell's equations does not involve time convolutions, as can be easily verified. However, in order to circumvent the convolutions due to the permittivity function, two new (hidden) field variables e_1 and e_3 are introduced. These are the analogues of the memory variables used in viscoelastic wave simulations to model dissipation from different attenuation mechanisms. Substituting the permittivity (4) and the conductivity (5) into equations (2) and (3), and following Carcione et al. (1988) yields

$$-\partial H_y/\partial z = \sigma_e E_x + \epsilon_e(\partial E_x/\partial t) + \epsilon^0 e_1 + J_x \quad , \tag{6}$$

$$\partial H_y/\partial x = \sigma_e E_z + \epsilon_e(\partial E_z/\partial t) + \epsilon^0 e_3 + J_z \quad , \tag{7}$$

where

$$\epsilon_e = \epsilon^\infty + \sigma^0\xi \tag{8}$$

and

$$\sigma_e = \sigma^0 + \epsilon^0\phi \tag{9}$$

are the effective optical permittivity and conductivity, respectively, with $\phi = (1 - \lambda/\tau)/\tau$. The third term of the right hand side in each equation involves the relaxation process through the corresponding hidden variable.

The radar equations are completed with the differential equations of the hidden variables:

$$\partial_t e_i = -(e_i + \phi E_i)/\tau \quad , \tag{10}$$

where $i = 1$ and $i = 3$ correspond to x and z, respectively.

Equations (1), (6) (7) and (10) are the basis of the numerical algorithm used to obtain the field vector $[H_y, E_x, E_z, e_1, e_3]$. A similar set of equations, but without Debye relaxation mechanisms and out-of-phase conduction currents, was solved by Carcione and Cavallini (1994).

The radar equations are solved with a direct grid method that computes the spatial derivatives using the Fourier pseudospectral method (Carcione and Cavallini, 1994) and propagates the solution in time with an explicit fourth-order Runge-Kutta algorithm. However, when there is a Debye peak whose central frequency is much larger than the dominant frequency of the source, the equations become stiff. In this case, a partition (or splitting) time integrator algorithm is used. The stiff part is solved analytically and the non-stiff part is solved with the Runge-Kutta algorithm. Details of this partition algorithm can be found in Carcione and Quiroga-Goode (1995), where Biot's poroelastic equations are solved.

BURIED CYLINDERS IN GRAVEL SAND

For this example, whose model is represented in Fig. 1, three cylindrical objects are buried in gravel. There are no dielectric relaxations and out-of-phase currents ($\lambda = \tau$ and $\xi = 0$, respectively), hence $\epsilon^0 = \epsilon^\infty \equiv \epsilon$ and $\sigma^0 \equiv \sigma$. The electromagnetic properties of the different materials are as follows:

Gravel sand: $\epsilon = 10.5 \ \epsilon_0$, $\sigma = 0.001$ mho/m;
Sand: $\epsilon = 8 \ \epsilon_0$, $\sigma = 0.0001$ mho/m;
Clay: $\epsilon = 7 \ \epsilon_0$, $\sigma = 0.01$ mho/m;
Plastic cylinder: $\epsilon = 4 \ \epsilon_0$, $\sigma = 0.0001$ mho/m;
Metal cylinder: $\epsilon = \epsilon_0$, $\sigma = 0.1$ mho/m;
Tree trunk: $\epsilon = 5 \ \epsilon_0$, $\sigma = 0.001$ mho/m,

where, in each case, ϵ_0 is the free-space dielectric constant. The numerical experiment simulates a stacked radargram obtained from the processing of a series of common 'shot' gathers (zero-offset profile). The source is an horizontal

electric current with a Ricker-type wavelet (e.g., Carcione and Cavallini, 1995) and a central frequency of 300 MHz. The wavefield is propagated with a time step of 0.05 ns and the receivers are located at the same level as the source.

The numerical mesh has $N_X = N_Z = 135$ grid points per side, with a uniform grid spacing of $D_X = D_Z = 7.5$ cm. In order to avoid wraparound caused by the Fourier differential operator, absorbing strips of length 18 grid points are used at the sides of the mesh (Kosloff and Kosloff, 1986). Fig. 2 represents a series of snapshots corresponding to the magnetic field H_y (left) and horizontal electric field E_x (right). At 20 ns the downgoing field has reached the cylinders, and the upgoing field is attenuated in the absorbing region. The snapshots at 30 and 40 ns show the diffraction of the incident plane wave by the cylinders (cylindrical wavefronts) which generates the hyperbolic-type reflection patterns in the radargrams displayed in Fig. 3. Note the different amplitude and phase behaviour of the reflection generated at the metal cylinder compared to the responses of the other cylinders. This figure can be compared with a similar published radargram obtained by Goodman (1994) using ray-tracing techniques.
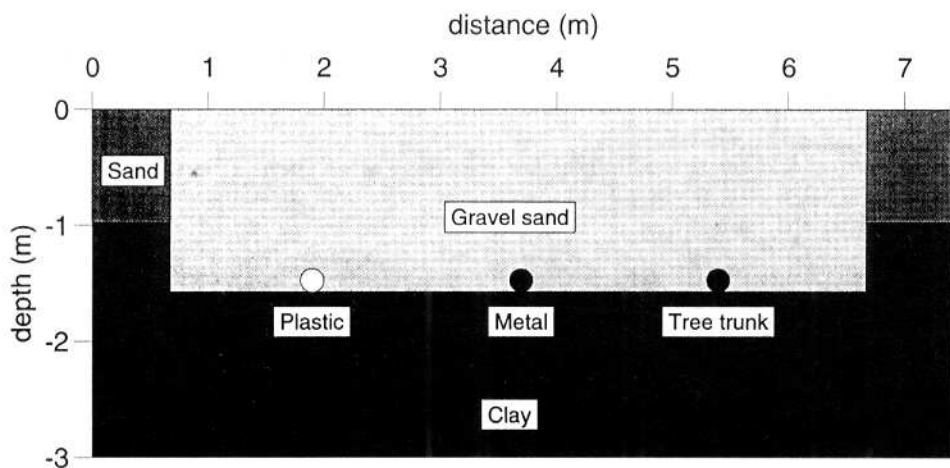
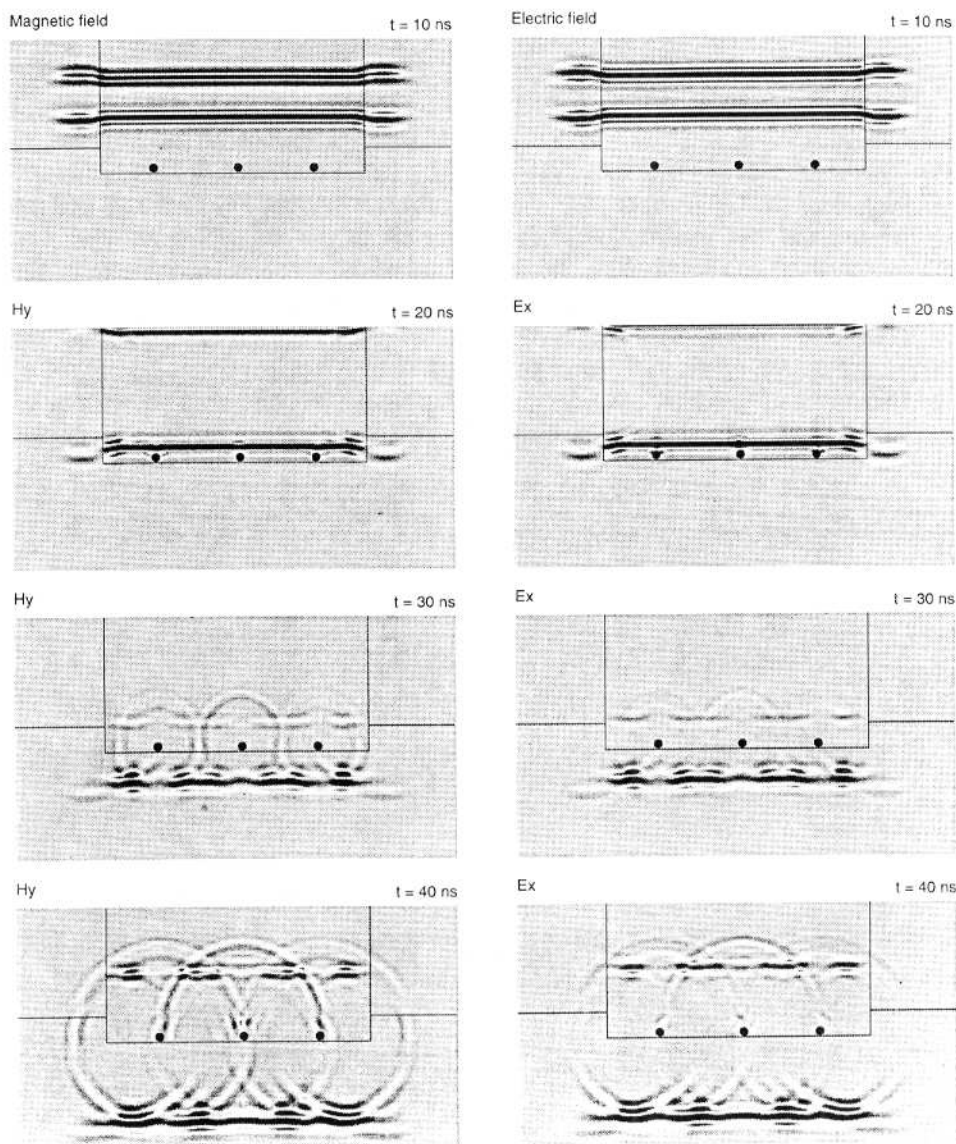Fig. 1. Model representing three buried cylinders in gravel sand.

Fig. 2. Sequence of snapshots corresponding to the magnetic field H_y (left) and the electric field component E_x (right) for the model represented in Fig. 1. The source is a horizontal electric current (plane wave) and its dominant frequency is 300 MHz.
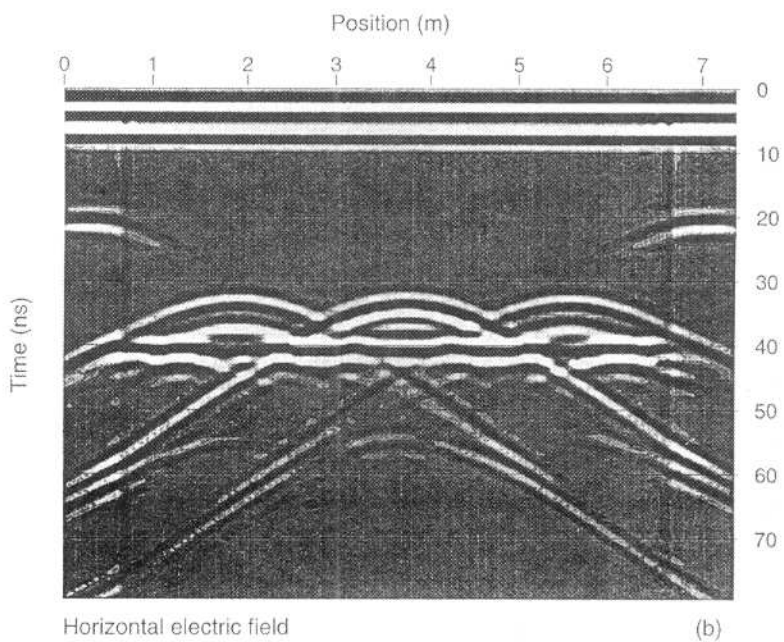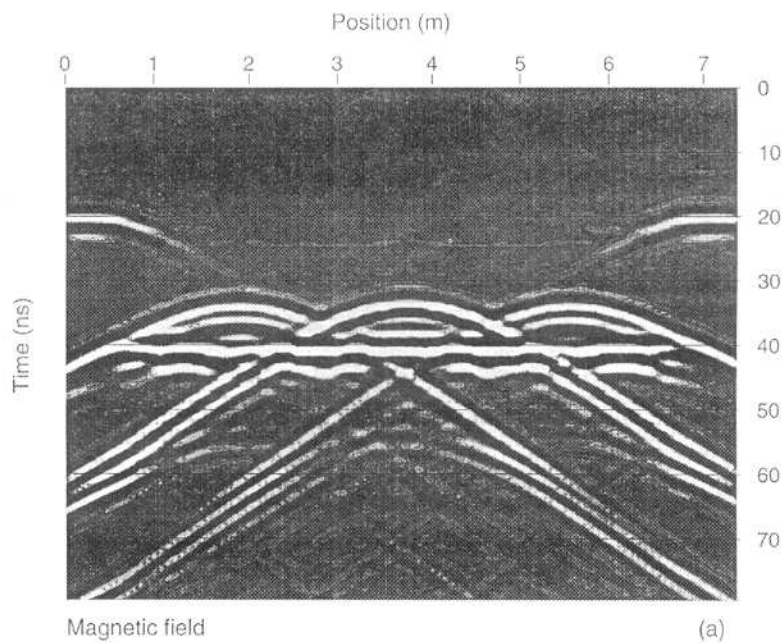
Fig. 3. Synthetic radargrams of the magnetic field H_y (a), and the horizontal electric field E_x (b). The model is given in Fig. 1 and the snapshots in Fig. 2.
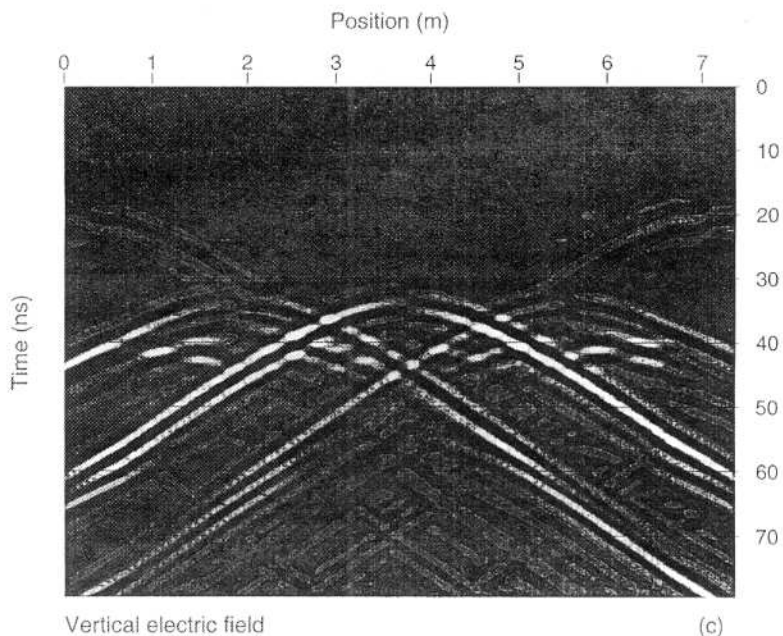
Position (m)

Vertical electric field   (c)

Fig. 3c. Synthetic radargram of the vertical electric field E_z. The model is given in Fig. 1 and the snapshots in Fig. 2.

ROAD BED WITH CAVITY

The model, introduced by Goodman (1994), represents an old concrete road that has been resurfaced (see Fig. 4). Some of the material properties are taken from Lau et al. (1992) who conducted the field experiment. Within this paper, a series of simulations are performed at different radar frequencies and material properties. The aim in performing the simulations is to analyze the radar resolution and the influence that realistic conductivity and permittivity functions have on the radargrams.

The electromagnetic properties are the following:

Asphaltic concrete: $\epsilon = 3.8\ \epsilon_0$, $\sigma = 0.02$ mho/m;
Portland concrete: $\epsilon^\infty = 5.3\ \epsilon_0$, $\sigma^0 = 0.03$ mho/m, $\xi = 0.148$ ns;
Asphalt: $\epsilon = 5.1\ \epsilon_0$, $\sigma = 0.002$ mho/m;
Void materials: air, $\epsilon = \epsilon_0$, $\sigma = 0.$; salt water, $\epsilon^\infty = 4.3\ \epsilon_0$,
                $\sigma^0 = 0.003$ mho/m, $\lambda = 0.0375$ ns, $\tau = 0.67$ ns;
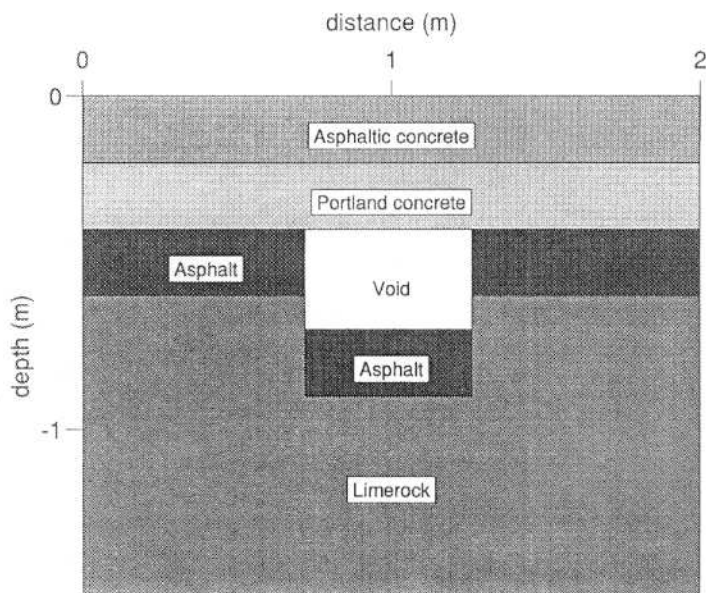Limerock: $\epsilon = 5.8\ \epsilon_0$, $\sigma = 0.3$ mho/m.

Fig. 4. Model representing a resurfaced roadbed containing a cavity.

The first simulation considers that the material in the cavity is air, and that $\xi = 0$ in the overlying Portland concrete. In this case, ϵ^∞ is taken equal to 5.8 ϵ_0, which equals ϵ_e when $\xi \neq 0$. The field is initiated by an horizontal electric current with a central frequency of 1.2 GHz, and is propagated with a time step of 0.02 ns. The numerical mesh has $N_x = N_z = 135$ grid points per side, with a uniform grid spacing of $D_x = D_z = 2$ cm. Fig. 5 represents the H_y radargram produced by a transmission antenna located above the road, and receivers distributed over the surface. The first and second reflection hyperbolae correspond to the bottom of the asphaltic and Portland concrete layers, respectively. The hyperbola corresponding to the base of the asphalt layer interferes with the response generated by the bottom of the cavity (at around 7.5ns), a response that has longer wavelength and shorter traveltime.

Fig. 6 shows the magnetic field radargram for different antennae frequencies: (a) 1.2 GHz, (b) 850 MHz, and (c) 500 MHz. The media are lossless ($\sigma = 0$, $\xi = 0$ and $\lambda = \tau$) and the simulation represents a zero-offset reflection profile (plane wave). Since the wave propagation process is linear, radargrams for different antennae frequencies are obtained with a single simulation by considering a space-time spike as perturbation and then performing the time convolution with the source time function. The reflection generated by the base of the Portland concrete layer (6 ns) is enhanced over the void region due to the high material contrast between the layer and the air.
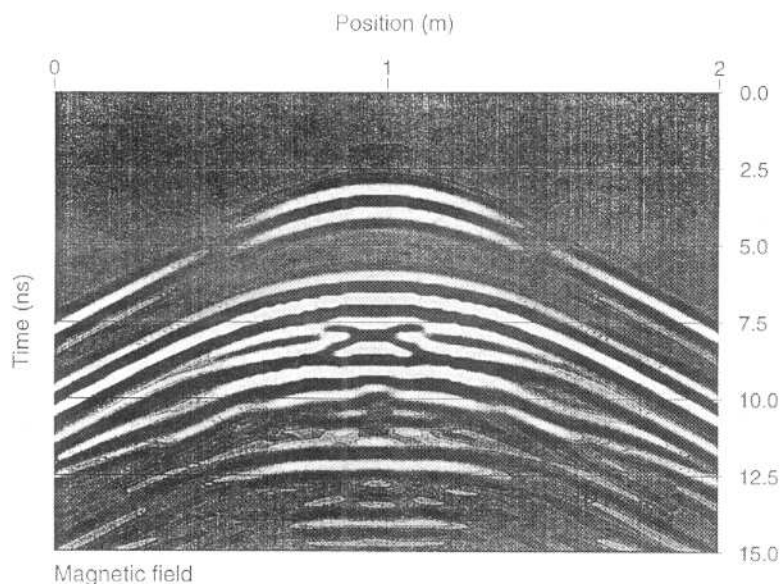
Fig. 5. Synthetic radargram of the magnetic field H_y corresponding to the roadbed model in the lossless case and the void filled with air. The source is a horizontal electric current (point source) and its dominant frequency is 1.2 GHz.
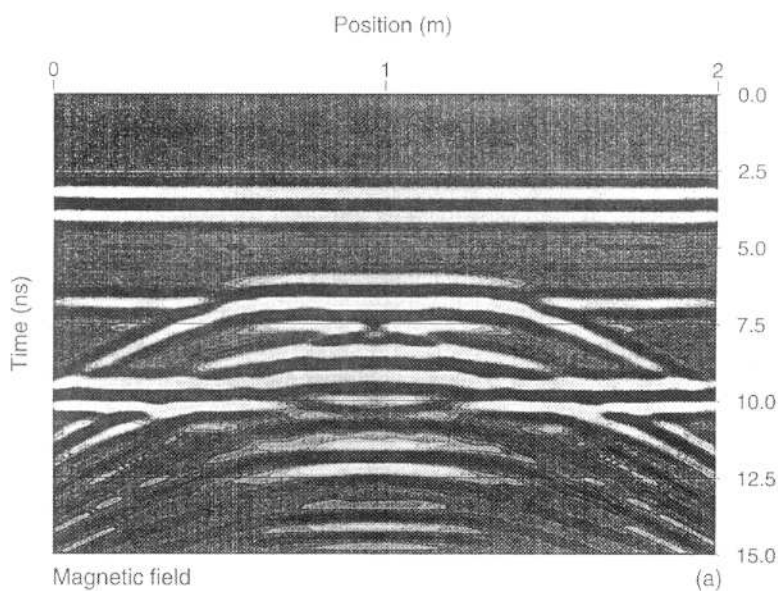

Fig. 6a. Magnetic field radargram for the antennae dominant frequency 1.2 GHz. The model is represented in Fig. 4, the media are lossless, the void is filled with air and the source is a horizontal electric current (plane wave).
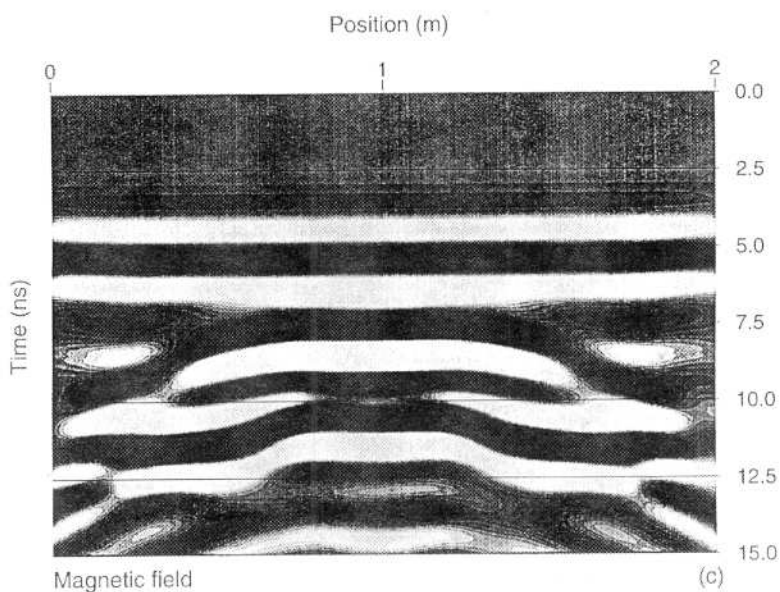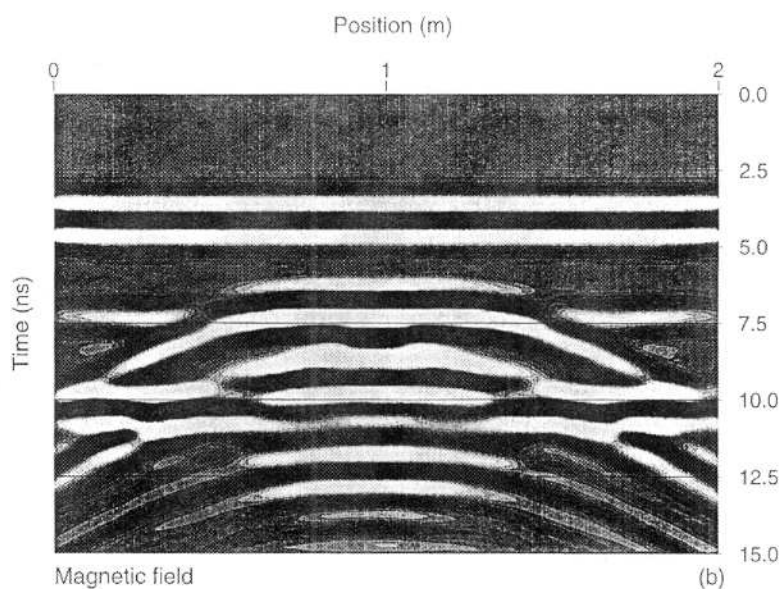
Fig. 6. Magnetic field radargrams for different antennae dominant frequencies: (b) 850 MHz and (c) 500 MHz. The model is represented in Fig. 4, the media are lossless, the void is filled with air and the source is a horizontal electric current (plane wave).

Moreover, the phase reversal observed by Goodman (1994) can be seen in the reflection generated from the upper part of the void. The responses from the bottom of the cavity, and the corresponding side reflections arrive at approximately 7.7 ns. The events from 9.5 to 12.5 ns correspond to the interference between the multiple reflection inside the cavity and the wave generated at the bottom of the lower asphalt layer. Fig. 6b still allows the identification of the single layers and the cavity, however this is not possible in Fig. 6c where the resolving power has substantially decreased.

In order to show the influence of the conductivity, Fig. 7 represents the radargrams with $\sigma \neq 0$, without out-of-phase conduction currents ($\xi = 0$) and dielectric relaxation ($\lambda = \tau$). Fig. 7a should be compared with Fig. 6a that has the same amplitude gain. As can be seen, the conductivity has considerably attenuated the wavefield. Increasing the amplitude by a factor 5.6 (Fig. 7b) restores the similarity to the lossless case.

Finally, consider the case where the void is filled with salt water and that $\xi \neq 0$ in the Portland concrete layer. The high attenuation properties of the salt water are modelled by a Debye relaxation peak centered at 1 GHz, defined by $\epsilon^\infty = 4.3 \, \epsilon_0$, $\tau = 0.67$ ns, and $\lambda = 0.0375$ ns. This gives a static dielectric constant $\epsilon^0 = 77.16 \, \epsilon_0$, a quality factor of 0.5 and a velocity of 9 cm/ns at 1.2 GHz. It can be shown, by a plane wave analysis of the TM equations, that the impermeability of the salt water is

$$\beta = [\tilde{\epsilon} - (i/\omega)\sigma^0]^{-1} \quad , \tag{11}$$

where

$$\tilde{\epsilon} = [(1+i\omega\lambda)/(1+i\omega\tau)]\epsilon^0 \quad , \tag{12}$$

with ω the angular frequency. Then, the quality factor and phase velocity can be calculated as

$$Q = \mathrm{Re}(V^2)/\mathrm{Im}(V^2) \tag{13}$$

and

$$V_p = [\mathrm{Re}(1/V)]^{-1} \quad , \tag{14}$$

respectively, where

$$V = (\beta/\mu_0)^{1/2} \tag{15}$$

is the complex velocity and the operators Re and Im take the real and imaginary parts, respectively. The frequency dependence of the dissipation (inverse of the quality factor Q) and phase velocity are represented in Figs. 8a and 8b, respectively. At low frequencies, the ionic conductivity dominates and the regime is diffusive (non-propagative). Alternatively, at radar frequencies, the presence of the Debye peak produces high dissipation in the cavity, as can be
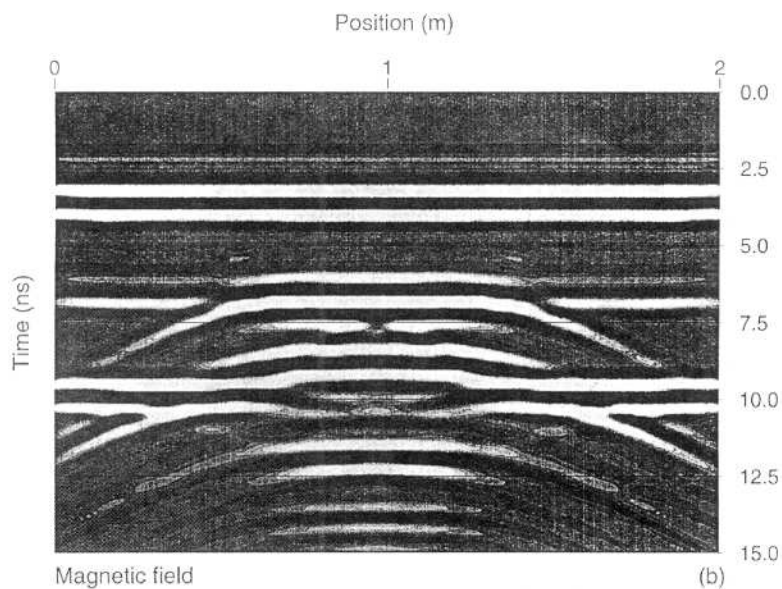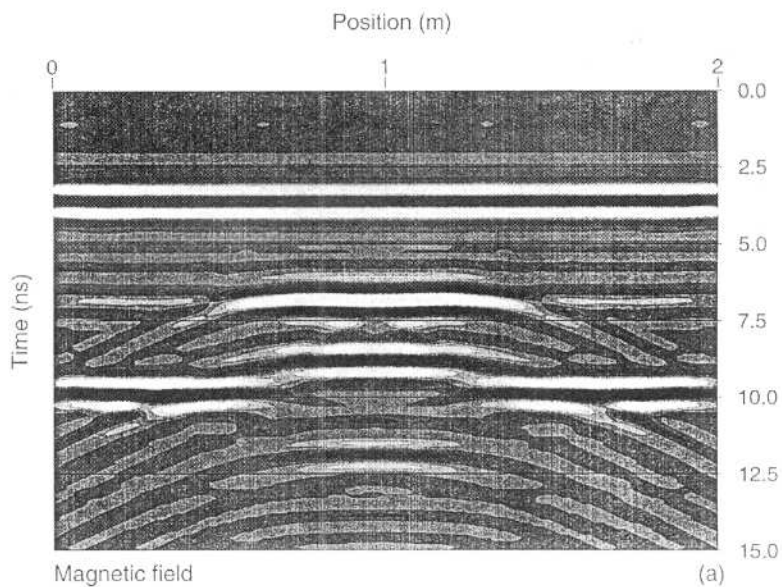
Fig. 7. Magnetic field radargrams as in Fig. 6a but including the conductivity properties. (a) has the same amplitude gain applied to the radargram shown in Fig. 6, and (b) has a gain factor of 5.6.
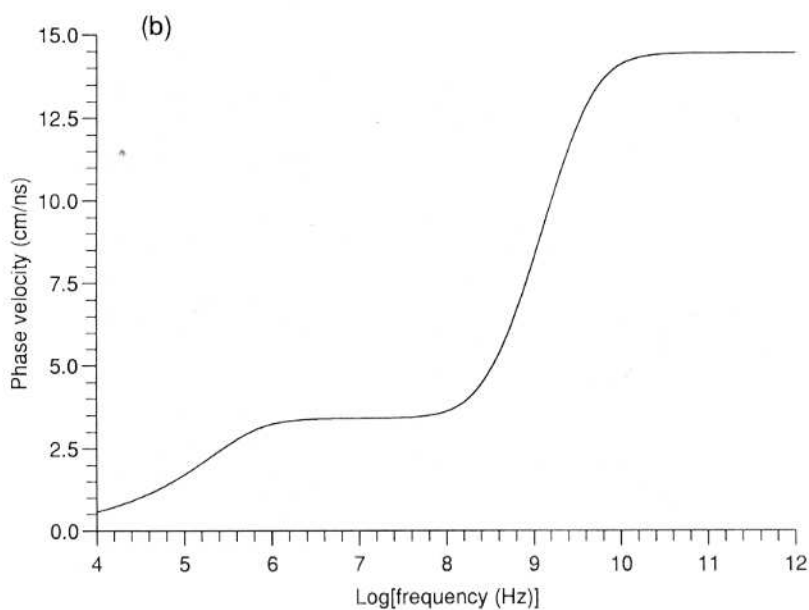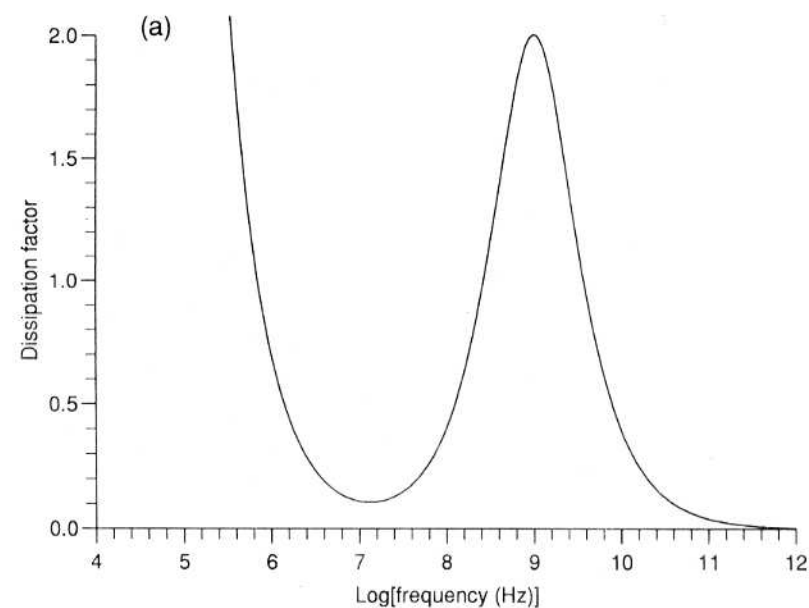
Fig. 8. Dissipation factor (a) and phase velocity (b) versus frequency, corresponding to salt water. A Debye relaxation peak is centered at 1 GHz.

appreciated in Fig. 9, which shows snapshots for the void filled with (a) air and (b) salt water. In the radargram (see Fig. 10), the high attenuation has eliminated the reflections corresponding to the bottom of the cavity and the asphalt layer below the void (compare with Fig. 7b).
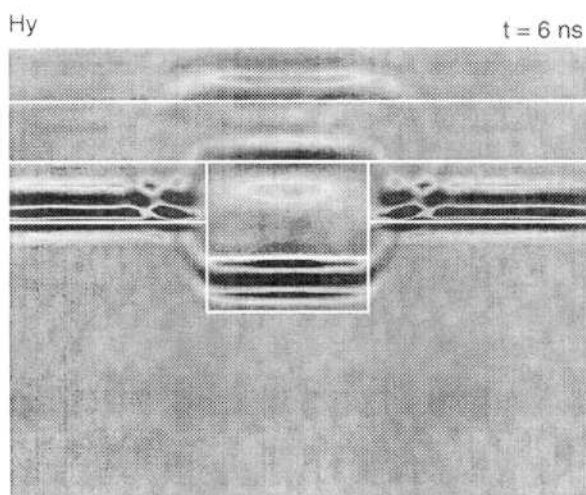
(a)
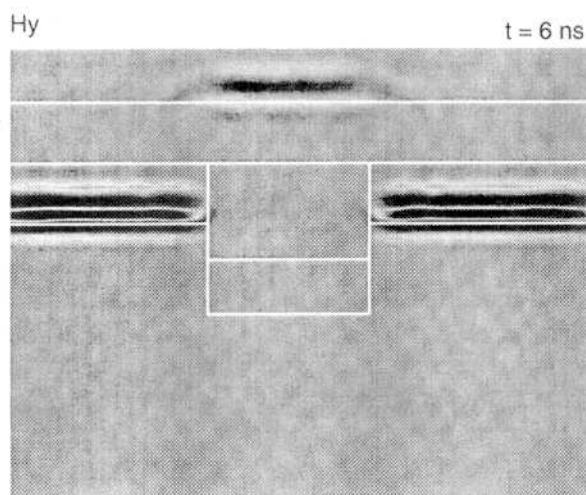
(b)

Fig. 9. Snapshots corresponding to roadbed model. In (a) the cavity is filled with air and in (b) with salt water. The source is a horizontal electric current (plane wave) and its dominant frequency is 1.2 GHz.
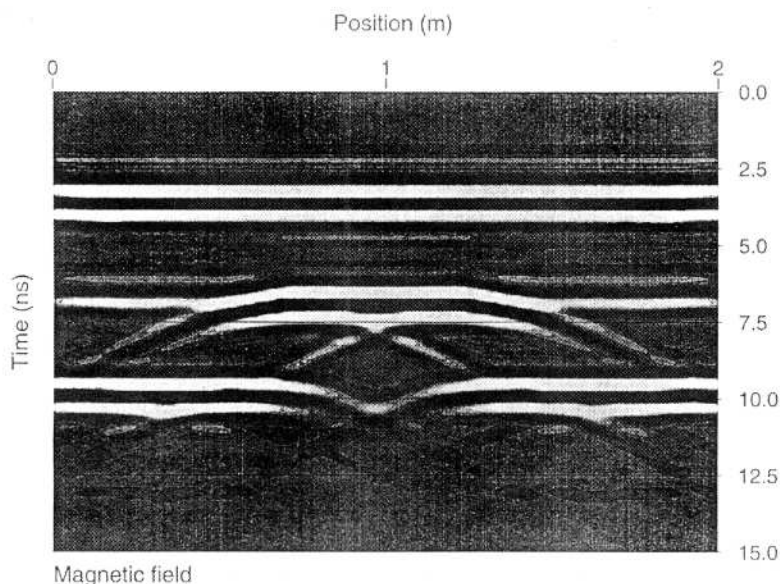
Position (m)

Fig. 10. Magnetic field radargram corresponding to Fig. 9b.

CONCLUSIONS

The correct description of the petrophysical and lithological properties play an important role when modeling radio waves in near-surface layers. In particular, ionic conductivity and dielectric relaxation processes have a significant influence on the attributes (amplitude and arrival time) of the radar pulses.

The proposed modeling technique uses a time-dependent formulation of the dielectric and conductivity properties, that accounts for the various dissipation mechanisms present in the radio-frequency band. In particular, the Debye relaxations require the introduction of hidden variables that are computed together with the electric and magnetic fields. The algorithm is based on the Fourier differential operator, and allows the calculation of the complete wavefield in arbitrarily inhomogeneous media.

Two applications show how the modeling can be used as an interpretation tool. The nature of the wavefield can be determined by computing snapshots at any propagation time. In this way, the reflections observed in the radargram can be easily interpreted.

Future research includes a detailed simulation of the antenna radiation pattern and extension of the theory and the modeling technique to the 3-D case.

REFERENCES

Carcione, J.M., Kosloff, D. and Kosloff, R., 1988. Visco-acoustic wave propagation simulation in the earth. Geophysics, 53, 769-777.
Carcione, J.M. and Cavallini, F., 1994. Modeling transverse electromagnetic waves in conducting anisotropic media by a spectral time-domain technique. In: Terzuoli, A. (Ed.), 10th Annual Review of Progress in Applied Computational Electromagnetics, Vol. II, pp. 586-593, Monterey, CA.
Carcione, J.M. and Cavallini, F., 1995. On the acoustic-electromagnetic analogy. Wave Motion, 21: 149-162.
Carcione, J. M. and Quiroga-Goode, G., 1995. Some aspects of the physics and numerical modeling of Biot compressional waves. J. Comput. Acoustics, 3: 261-280.
Goodman, D., 1994. Ground-penetrating radar simulation in enginnering and archaeology. Geophysics, 59: 224-232.
Hasted, J.B., 1973. Aqueous Dielectrics. Chapman and Hall, London.
Lau, C.L., Scullion, T. and Chan, P., 1992. Using ground-penetrating radar technology for pavement evaluations in Texas, U.S.A. Finland Geol. Sur., 4th Internat. Conf. on Ground-Penetrating Radar, special paper 16: 277-283.
Kosloff, R. and Kosloff, D., 1986. Absorbing boundaries for wave propagation problems. J. Comput. Phys., 63: 363-376.
Owen, T.E. (Ed.), 1995. Special Issue on Ground-Penetrating Radar. J. of Appl. Geophys., 33: 1-225.
Zener, C., 1948. Elasticity and Anelasticity of Metals. University of Chicago Press, Chicago, Illinois.